

A Variational Approach to Chiral Topological Order Interfaces

V. Crépel¹, N. Claussen¹, B. Estienne², N. Regnault¹

¹*Laboratoire Pierre Aigrain, Ecole normale supérieure,
PSL University, Sorbonne Université, Université Paris Diderot,
Sorbonne Paris Cité, CNRS, 24 rue Lhomond, 75005 Paris France and*

²*Sorbonne Université, CNRS, Laboratoire de Physique Théorique et Hautes Énergies, LPTHE, F-75005 Paris, France*

Interfaces between two topologically distinct phases of matter reveal a remarkably rich phenomenology. To go beyond effective field theories, we study the prototypical example of such an interface between two Abelian states, namely the Laughlin and Halperin states. Using matrix product states, we propose a variational ansatz for the whole system including both the bulks and the interface. We show through extensive numerical studies that it unveils both the universal properties of the system, such as the central charge of the gapless interface mode, and its microscopic features. It also captures the low energy physics of experimentally relevant Hamiltonians. Our approach can be generalized to other phases described by tensor networks.

Introduction — The Integer Quantum Hall (IQH) effect, characterized by the quantization of the Hall conductance in units of e^2/h , can occur even in the absence of a uniform magnetic field and requires neither flat bands nor Landau levels [1]. From a band-theory point of view, the difference between a trivial band insulator and the IQHE stems from the subtle sensitivity to boundary conditions. This is encoded in the first Chern integer \mathcal{C} [2] which depends on the topology of the valence band bundle. This quantized invariant forbids the adiabatic transformation of the IQHE into any trivial band insulator without undergoing a quantum phase transition [3]. Such a transition occurs for instance at the edge of an IQH droplet, which is nothing but an interface with the vacuum. The closure of the gap is manifest in the presence of conducting channels at the edge, and the corresponding Hall conductance $\mathcal{C}e^2/h$ yields a measure of the Chern number \mathcal{C} . The insulating bulk completely determines the gapless theory at the interface with a topologically trivial phase. Strongly correlated phases with intrinsic topological order such as the Fractional Quantum Hall (FQH) effect share the same features : bulk global invariants control the nature of the gapless interface at the transition to a trivial phase.

Conversely, the *Bulk-Edge Correspondence* conjectures that the gapless theory at such a transition governs the full topological content of the FQH state. This conjecture was considerably substantiated by the pioneering work of Moore and Read [4] who expressed a large class of FQH model Wave Functions (WFs) as Conformal Field Theory (CFT) correlators. This CFT is chosen to match the one used to describe the gapless edge modes of the target state, making the correspondence between the bulk and edge properties transparent. It provides many insights into the study of these strongly correlated phases [5–9].

At the transition between two phases with distinct intrinsic topological order, the critical theory has no reason to be described by the same formalism. Indeed, only the "difference" in topological content of the two bulks is probed at such a gapless interface. For instance, the Hall

conductance at the interface between two IQH plateaus is $\Delta\mathcal{C}e^2/h$, and is controlled by the difference in Chern numbers $\Delta\mathcal{C}$. The notion of difference should be refined for strongly interacting systems such as FQH states. But even for the IQH, it cannot completely characterize the two bulks. As a consequence, even the transitions between Abelian states have not yet been classified [10–12]. However, for interfaces with the same number of left and right movers, the topologically distinct ways of gapping the boundary were mathematically distinguished as "Lagrangian subgroups" [13, 14].

Theoretical approaches to understanding these transitions mostly rely on the "cut and glue" approach [15], *i.e.* restricting the analysis to coupled one dimensional modes. In this effective picture, both phases are solely described by their respective edge theory, and the interface emerges from the coupling between the two edge theories [16, 17]. On the CFT side, this approach refines the notion of "difference" in topological content with the help of coset constructions [18, 19]. In this article, we aim to put the above effective edge approaches on firmer ground by analysing the full two-dimensional problem of topological interfaces. To do so, we introduce variational WF's describing the interface between two Abelian states, namely the Laughlin [20] and Halperin [21] states. Having a description of the full two-dimensional system, we can unveil both the universal properties *and* the microscopic features. We provide extensive numerical studies to probe the full critical theory at the interface, and to demonstrate that these 2D WF's correctly capture the physics of both bulks and of the interface.

Setup — The Halperin $(m, m, m-1)$ state with m integer (even for bosons and odd for fermions) appears at a filling factor $\nu = \frac{2}{2m-1}$. It describes an FQH fluid with an internal two-level degree of freedom [21, 22] such as the spin, the valley degeneracy in graphene or the layer index in bilayer systems. In the following, we use the terminology of the spin degree of freedom irrespectively of the actual physical origin. Such a state is the natural spin singlet [23–25] generalization of the celebrated, spin

polarized, Laughlin state [20, 26]. The later describes an FQH state at filling factor $\nu = 1/m$. From now on, we will focus on bosons and $m = 2$, as this already realizes all the non-trivial physics we put forward in this article. In that case, both the Halperin (221) and the Laughlin $1/2$ states are the densest zero energy states of the following Hamiltonian projected onto the Lowest Landau Level (LLL) [27, 28]:

$$\mathcal{H}_{\text{int}} = \int d^2\mathbf{r} \sum_{\sigma, \sigma'=\uparrow, \downarrow} : \rho_{\sigma}(\mathbf{r}) \rho_{\sigma'}(\mathbf{r}) : + \mu_{\uparrow} \rho_{\uparrow}(\mathbf{r}) \quad (1)$$

respectively for $\mu_{\uparrow} = \infty$ and $\mu_{\uparrow} = 0$. Here μ_{\uparrow} is a chemical potential for the particles with a spin up, ρ_{σ} denotes the density of particles with spin component σ , and $: \cdot :$ stands for normal ordering. Hence, creating an interface between these two topologically ordered phases can be achieved by making μ_{\uparrow} spatially dependent without tuning the interaction [18].

The Laughlin and Halperin model WFs can also be defined by CFT correlators [4, 29]. Both states are Abelian, and the primaries appearing in the correlators are vertex operators [9, 30–33]. The mode expansion of the primaries in the correlators allow for an exact MPS description of the WFs over the Landau orbitals [34–37]. On the cylinder geometry, Landau orbitals are shifted copies of a Gaussian envelope whose center is determined by the momentum along the compact dimension (see Fig. 1a). Because of this emergent translation symmetry on the cylinder geometry, the exact MPS representation of the model WFs can be made site independent which enables the use of efficient infinite-MPS (iMPS) algorithms [38–40]. The auxiliary space, *i.e.* the Hilbert space associated to the matrix indices, is the truncated CFT Hilbert space used for the Halperin state, a two-component compactified boson [37]. Similarly, the CFT Hilbert space for the Laughlin state is made of a single compactified boson. By choosing the same m for the two model WFs, it is possible to embed the auxiliary space of the Laughlin state in that of the Halperin state. This property is the key to our variational approach of the interface between two phases. The Laughlin state is obtained after polarizing the system in its spin down component, as previously stated (see Eq. 1). Accounting for the block structure with respect to the $U(1)$ -charges and momentum of the two bosons provides additional refinement and enhances the efficiency of the iMPS machinery [41]. The truncation of the auxiliary space is constrained by the entanglement area law [42], the bound dimension should grow exponentially with the cylinder perimeter L to accurately describes the model WFs.

Variational Wavefunction — Our variational ansatz for the transition consists in using the Halperin iMPS matrices for any Landau orbital whose center is in the unpolarized region $x < 0$, and the Laughlin iMPS matrices when $x > 0$, as sketched in Fig. 1a. This ansatz

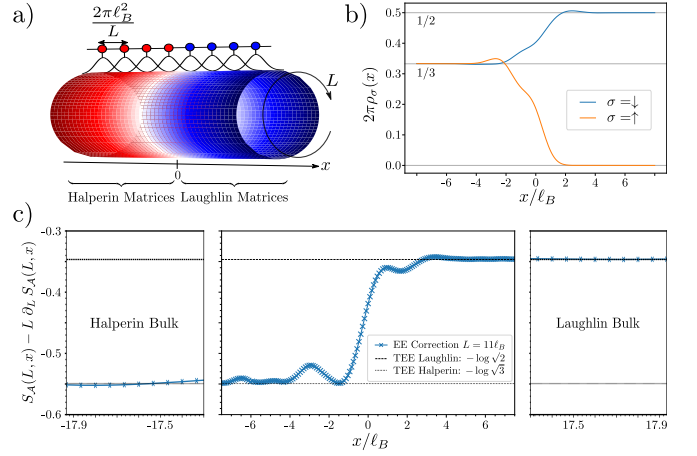


FIG. 1. a) Sketch of our variational MPS ansatz for the interface between an Halperin and a Laughlin state. The Halperin MPS matrices (red circles) are glued to the Laughlin MPS matrices (blue circles) in the Landau orbital space. The momentum along the compact direction y labels the Landau orbitals and determines the center of their Gaussian envelope on the cylinder. b) Spin resolved densities of the variational Ansatz state along the cylinder axis. They smoothly interpolate between the Laughlin ($2\pi\rho_{\downarrow} = 1/2$ and $\rho_{\uparrow} = 0$) and the Halperin ($2\pi\rho_{\downarrow} = 2\pi\rho_{\uparrow} = 1/3$) theoretical values. The persistent density inhomogeneity is an edge reconstruction due to interactions (see Eq. 1). c) Constant correction of the EE to the area law for a rotationally symmetric bipartition at position x . The correction is found to be constant (see Eq. 2). The extraction of the TEE deep in the Laughlin and Halperin bulks shows that the MPS variational ansatz correctly captures the topological properties away from the interface.

may be understood as an abrupt change of the chemical potential μ_{\uparrow} from zero to infinity in orbital space, which maps to a smooth Gaussian ramp in real space over a distance $2\pi\ell_B^2/L$, ℓ_B being the magnetic length. A direct probe of this polarization is seen in the spin resolved densities ρ_{\uparrow} and ρ_{\downarrow} of the variational ansatz presented in Fig. 1b for the transition between the Halperin (221) and the Laughlin $1/2$ states. They smoothly interpolate between the polarized Laughlin bulk at filling factor $\nu_L = 1/2$ and the Halperin unpolarized bulk at filling factor $\nu_H = \frac{1}{3} + \frac{1}{3}$. We recover the typical bulk densities and the spin symmetry of the Halperin (221) state after a few magnetic lengths, which is much larger than the distance between orbitals. This is not an artifact of our ansatz since Exact Diagonalization (ED) simulations of Eq. 1 for a half polarized system with delta interactions show the same behaviour [41]. The density inhomogeneity at the interface is a probe of the interface reconstruction due to interactions (see Eq. 1).

The MPS description naturally separates the different topological sectors of both the Halperin and the Laughlin states. Since no local measurement should distinguish between the topological sectors, they are only determined by the $U(1)$ -charges of the MPS boundary states. While

for the Halperin state, the U(1)-charges and the level descendants (or momenta) of both auxiliary bosons should be fixed, only one of each is required to determine the Laughlin topological sector. The remaining boson at the edge of the Laughlin bulk constitutes a knob to dial the states of the one dimensional edge mode at the interface.

Numerical results — A crucial feature that our ansatz should reproduce is the topological order of the Halperin and Laughlin bulks away from the transition, *i.e.* when $|x| \gg \ell_B$. Local operators such as the density cannot probe the topological content of the bulks. We thus rely on the entanglement entropy (for a review, see Ref. [43]) to analyze the topological features of our model WF. Consider a bipartition $\mathcal{A} - \mathcal{B}$ of the system defined by a cut perpendicular to the cylinder axis at a position x . The Real-Space Entanglement Spectrum (RSES) [44–46] and the corresponding Von Neumann EE $S_A(L, x)$ are computed for various cylinder perimeters L using techniques developed in Refs. [34, 36, 37]. Two dimensional topological ordered phases satisfy the area law [42]

$$S_A(L, x) = \alpha(x)L - \gamma(x) \quad (2)$$

where $\alpha(x)$ is a non universal constant and $\gamma(x)$ is the Topological Entanglement Entropy (TEE). The latter is known to characterize the topological order [47, 48]. Since the cylinder perimeter is a continuous parameter in our simulations, we extract these constants by numerically computing the derivative $\partial_L S_A(L, x)$ as depicted in Fig. 1c for $\gamma(x)$. Deep in the bulks, our results match the theoretical prediction for the Laughlin ($\gamma(x \rightarrow +\infty) = \log \sqrt{m}$) and Halperin ($\gamma(x \rightarrow -\infty) = \log \sqrt{2m-1}$) states. This proves the validity of our ansatz away from the interface.

Near the transition, the EE still follows Eq. 2 as was recently predicted for such a rotationally invariant bipartition [16]. The correction $\gamma(x)$ smoothly interpolates between its respective Laughlin and Halperin bulk values (see Fig. 1c). Hence, it contains no universal signature of the critical mode at the interface between the two topologically ordered phases. The same conclusion holds for the area law coefficient $\alpha(x)$ [41].

We now focus on the critical mode that should lie at the interface. Effective one-dimensional theories similar to the ones of Refs. [18, 19, 49] predict that the gapless interface is described by a free bosonic CFT, denoted as φ_{edge} , of central charge $c = 1$ and compactification radius $R_{\text{edge}} = \sqrt{m(2m-1)}$ [30] which is neither an edge mode of the Halperin state nor of the Laughlin state. It may be understood as follows: the edge of the Halperin FQH droplet is a spinful Luttinger liquid in which spin and charge excitations separate into two independent bosonic excitations denoted as φ_c and φ_s . Because the interface presented is fully transmissive to spin down electrons, backscattering processes [49] gap out the combination of spin and charge bosons relative to spin down electrons.

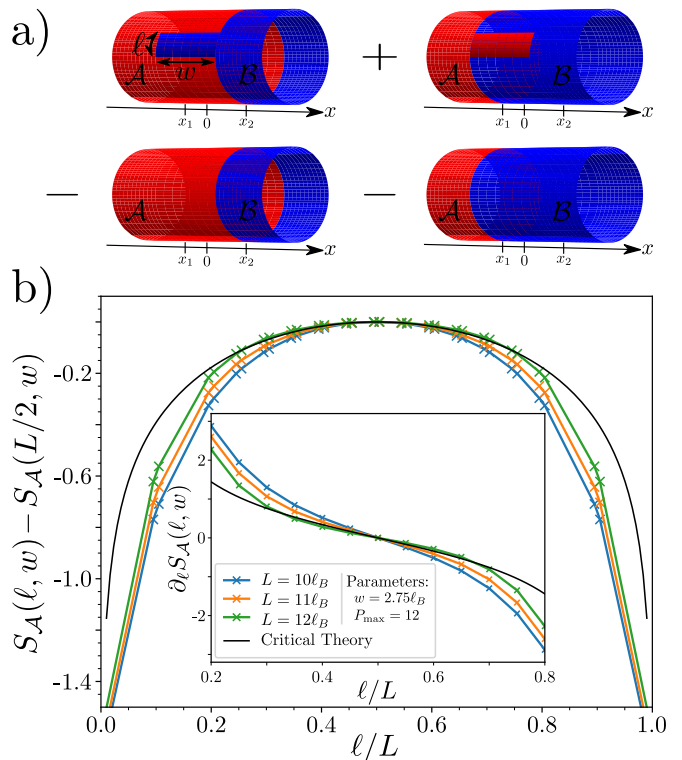


FIG. 2. a) *Levin-Wen subtraction scheme* to get rid off the spurious area law coming from the patch boundaries along the cylinder perimeter together with corner contributions to the EE. The position and width w of the rectangular extension are selected to fully include the gapless mode at the interface. The critical EE coming from the gapless mode at the interface is counted twice. b) $S_A(\ell, w)$ for different cylinder perimeters. They all fall on top of the CFT prediction Eq. 4, pointing toward a critical chiral edge mode at the interface. The inset shows the derivative $\partial_\ell S_A(\ell, w)$ and its agreement with the theoretical prediction.

What remains is the non-trivial bosonic field

$$\varphi_{\text{edge}} = \sqrt{\frac{1}{2m}} \varphi_c + \sqrt{\frac{2m-1}{2m}} \varphi_s \quad (3)$$

To test this one dimensional effective theory, we compute the RSES for a bipartition for which the part \mathcal{A} consists of a rectangular patch of length ℓ along the compact dimension and width w along the x -axis, *i.e.* we break the rotational symmetry along the cylinder perimeter. To fully harness the power of the iMPS approach, it is convenient to add a half infinite cylinder to the rectangular patch (see Fig. 2a). The technical challenges inherent to such a computation breaking spatial symmetries are presented in Ref. [41]. We isolate the contribution of the interface edge mode from the area laws and corner contributions with a Levin-Wen addition subtraction scheme [48] depicted in Fig. 2a. Note that it counts the contribution of the gapless interface to the EE twice and that a spurious contribution due to short range entanglement along the cut parallel to the x -axis may appear.

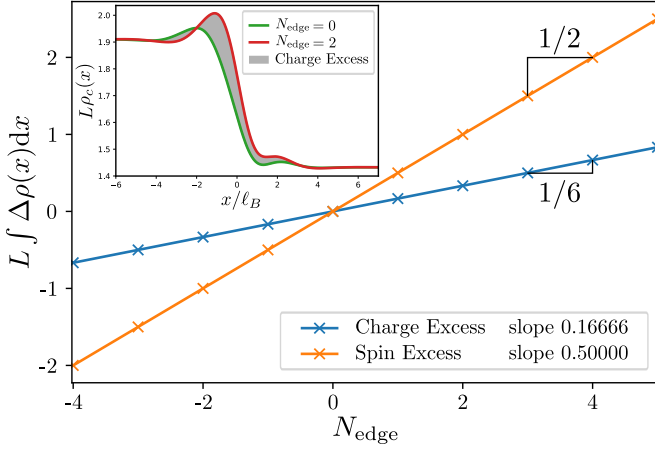


FIG. 3. Charge (in blue) and spin (in orange) excess $L \int \Delta\rho(x)dx$ are localized at the interface when excited states are addressed via the MPS boundary $U(1)$ charge N_{edge} . Inset shows how to extract the charge excess (gray shaded area) from the charge densities ρ_c at different N_{edge} . Each excess follows a linear relation with extremely good accuracy. The charge (resp. spin) excess has a slope $0.166662(5) \simeq 1/6$ (resp. $0.500005(5) \simeq 1/2$). This indicates that the elementary excitations of the $c = 1$ critical theory (cf Fig. 2) at the interface carry a fractional charge $e/6$ and a fractional spin $1/2$ in unit of the electron spin.

We vary the length ℓ along the compact dimension of the cylinder while keeping w constant. In Fig. 2b, we observe that the EE $S_A(\ell, w)$ resulting from the Levin-Wen scheme shown in Fig. 2a follows the 1D prediction for a chiral $c = 1$ CFT with periodic boundary conditions [50]

$$S_A(\ell, w) - S_A(L/2, w) = 2 \frac{c}{6} \log \left[\sin \left(\frac{\pi \ell}{L} \right) \right] \quad (4)$$

To be more quantitative, we fit the numerical derivative $\partial_\ell S_A(\ell, w)$ with the theoretical prediction using the central charge c as the only fitting parameter (the derivative removes the area law contribution arising from the cut along x). We minimize finite size effects by keeping only the points for which ℓ and $L - \ell$ are both greater than four times the Halperin (221) bulk correlation length [37]. Fitting the data obtained for a perimeter $L = 12\ell_B$ (the largest L that reliably converges with the the largest reachable auxiliary space), we find $c \simeq 0.987(1)$ (see Fig. 2). We verified that the rectangular patch was covering entirely the gapless mode by checking that the results hold for a large range of w [41]. Moreover, performing the same calculation far away in the gapped Laughlin phase leads to a fitted value of $c \leq 0.13$.

In order to fully characterize the gapless mode at the interface, we now extract the charges of its elementary excitations which are related to the compactification radius R_{edge} . As previously mentioned, excited states of the critical theory are numerically controlled by the $U(1)$ -charge N_{edge} which is part of the MPS boundary con-

dition on the Laughlin side. For each of these excited states, we compute the spin resolved densities and observe that the excess of charge and spin are localized around the interface (see inset of Fig. 3). They stem from the gapless interface mode observed in Fig. 2b and we plot the charge and spin excess as a function of N_{edge} in Fig. 3. The linear relation indicates that the interface critical theory hosts excitations carrying a fractional charge $e/6$ and a fractional spin $1/2$ in units of the electron spin. Physically [18], a Laughlin $1/2$ quasihole carrying an electric charge $e/2$ passing through the transition region can excite an elementary Halperin (221) quasihole of charge $e/3$ but $e/6$ charge has to be absorbed by the gapless mode at the interface.

Microscopic model and experimental realizations — While our ansatz has the desired features to describe the low energy physics of Eq. 1, we can provide a more quantitative comparison. As opposed to a Halperin state with a macroscopic number of quasiholes in the polarized region (as discussed in Ref. [18]) which completely screens the Hamiltonian Eq. 1, the critical edge mode at the interface now acquires a finite energy. But this low energy mode clearly detaches from the continuum, allowing us to compare it to our ansatz in finite size studies using exact diagonalization. The largest accessible system size involves 13 bosons, 9 with spin down and 4 with spin up, interacting with delta potentials over 21 orbitals, 9 of which are completely polarized. We find extremely good agreement between the ED ground state and our MPS ansatz, with an overlap of 0.9989. This provides a clear evidence of its physical relevance. Changing the level descendant P_{edge} of the φ_{edge} boson, which is dialed through the MPS boundary condition on the Laughlin side, we were able to reproduce the first few low lying excitations of the system above the finite size ground state with similar accuracy [41]. Using matrix product operators and our ansatz, we can actually focus on and evaluate the dispersion relation of the gapless interface mode [41].

We also considered the fermionic transition between the Laughlin $1/3$ and Halperin (332) states which is more relevant for condensed matter experiments [41]. It exhibits the same features as the bosonic case previously discussed: the gapless mode at the interface is described by a bosonic $c = 1$ CFT φ_{edge} whose elementary excitations agree with the value of R_{edge} . In the later case, experimental realization of this transition might be envisioned in graphene. There, the valley degeneracy leads to a spin singlet state at $\nu = 2/5$ [51, 52] while the system at $\nu = 1/3$ is spontaneously valley-polarized [52–54]. Thus, changing the density through a top gate would provide a direct implementation of our setup.

Conclusion — Our variational ansatz not only captures the bulk topological content of the FQH states glued together, but it also faithfully describes the gapless interface theory, as shown by the extensive numerical

analysis presented in this article. This gapless $c = 1$ theory hosts fractional elementary excitations which are neither Laughlin nor Halperin quasiholes, a probe of the interface reconstruction due to interactions. Although the universal properties can be inferred from one dimensional effective theories [13, 49, 55], our ansatz validates such an approach while granting access to a full microscopic characterization. It also accurately matches the low energy physics of experimentally relevant microscopic Hamiltonians. Our approach can be extended to topologically ordered phases described by MPS or any tensor network method, paving the way to a deeper understanding of interfaces between such phases.

Acknowledgments — We thank E. Fradkin, J. Dubail, A. Stern and M.O. Goerbig for enlightening discussions. We are also grateful to B.A. Bernevig and P. Lecheminant for useful comments and collaboration on previous works. V.C., B.E. and N.R. were supported by the grant ANR TNSTRONG No. ANR-16-CE30-0025.

-
- [1] F. D. M. Haldane, Phys. Rev. Lett. **61**, 2015 (1988).
 - [2] D. J. Thouless, M. Kohmoto, M. P. Nightingale, and M. den Nijs, Phys. Rev. Lett. **49**, 405 (1982).
 - [3] X. Chen, Z.-C. Gu, and X.-G. Wen, Phys. Rev. B **82**, 155138 (2010).
 - [4] G. Moore and N. Read, Nucl. Phys. B **360**, 362 (1991).
 - [5] B. Blok and X. Wen, Nucl. Phys. B **374**, 615 (1992).
 - [6] Y.-L. Wu, B. Estienne, N. Regnault, and B. A. Bernevig, Phys. Rev. B **92**, 045109 (2015).
 - [7] Y.-L. Wu, B. Estienne, N. Regnault, and B. A. Bernevig, Phys. Rev. Lett. **113**, 116801 (2014).
 - [8] B. Estienne, Z. Papić, N. Regnault, and B. A. Bernevig, Phys. Rev. B **87**, 161112 (2013).
 - [9] T. H. Hansson, M. Hermanns, S. H. Simon, and S. F. Viefers, Rev. Mod. Phys. **89**, 025005 (2017).
 - [10] A. Kapustin and N. Saulina, Nucl. Phys. B **845**, 393 (2011).
 - [11] A. Kitaev and L. Kong, Communications in Mathematical Physics **313**, 351 (2012).
 - [12] J. Fuchs, C. Schweigert, and A. Valentino, Communications in Mathematical Physics **321**, 543 (2013).
 - [13] M. Levin, Phys. Rev. X **3**, 021009 (2013).
 - [14] M. Barkeshli, C.-M. Jian, and X.-L. Qi, Phys. Rev. B **88**, 241103 (2013).
 - [15] X.-L. Qi, H. Katsura, and A. W. W. Ludwig, Phys. Rev. Lett. **108**, 196402 (2012).
 - [16] L. H. Santos, J. Cano, M. Mulligan, and T. L. Hughes, ArXiv e-prints (2018), arXiv:1803.04418 [cond-mat.str-el].
 - [17] C. L. Kane, R. Mukhopadhyay, and T. C. Lubensky, Phys. Rev. Lett. **88**, 036401 (2002).
 - [18] E. Grosfeld and K. Schoutens, Phys. Rev. Lett. **103**, 076803 (2009).
 - [19] Y. Hu and C. L. Kane, Phys. Rev. Lett. **120**, 066801 (2018).
 - [20] R. B. Laughlin, Phys. Rev. Lett. **50**, 1395 (1983).
 - [21] B. Halperin, Helv. Acta Phys. **56**, 75 (1983).
 - [22] B. I. Halperin, Phys. Rev. Lett. **52**, 1583 (1984).
 - [23] A. P. Sankar Das Sarma, *Perspectives in Quantum Hall Effects: Novel Quantum Liquids in Low-Dimensional Semiconductor Structures* (WILEY-VCH Verlag, 2007).
 - [24] Z. Papić, *Fractional quantum Hall effect in multicomponent systems*, These, Université Paris Sud - Paris XI (2010).
 - [25] R. de Gail, N. Regnault, and M. O. Goerbig, Phys. Rev. B **77**, 165310 (2008).
 - [26] E. H. Rezayi and F. D. M. Haldane, Phys. Rev. B **50**, 17199 (1994).
 - [27] S. A. Trugman and S. Kivelson, Phys. Rev. B **31**, 5280 (1985).
 - [28] F. D. M. Haldane, Phys. Rev. Lett. **51**, 605 (1983).
 - [29] S. Fubini, Modern Physics Letters A **06**, 347 (1991).
 - [30] P. D. Francesco, P. Mathieu, and D. Sénéchal, *Conformal Field Theory* (Springer-Verlag New York, 1997).
 - [31] G. Cristofano, G. Maiella, R. Musto, and F. Nicodemi, Modern Physics Letters A **6**, 1779 (1991).
 - [32] G. Cristofano, G. Maiella, R. Musto, and F. Nicodemi, Physics Letters B **262**, 88 (1991).
 - [33] G. Cristofano, G. Maiella, R. Musto, and F. Nicodemi, Modern Physics Letters A **06**, 2985 (1991).
 - [34] M. P. Zaletel and R. S. K. Mong, Phys. Rev. B **86**, 245305 (2012).
 - [35] J. Dubail, N. Read, and E. H. Rezayi, Phys. Rev. B **86**, 245310 (2012).
 - [36] B. Estienne, N. Regnault, and B. A. Bernevig, ArXiv e-prints (2013), arXiv:1311.2936 [cond-mat.str-el].
 - [37] V. Crépel, B. Estienne, B. A. Bernevig, P. Lecheminant, and N. Regnault, Phys. Rev. B **97**, 165136 (2018).
 - [38] M. P. Zaletel, R. S. K. Mong, and F. Pollmann, Phys. Rev. Lett. **110**, 236801 (2013).
 - [39] M. P. Zaletel, R. S. K. Mong, and F. Pollmann, Phys. Rev. Lett. **110**, 236801 (2013).
 - [40] M. P. Zaletel, R. S. K. Mong, F. Pollmann, and E. H. Rezayi, Phys. Rev. B **91**, 045115 (2015).
 - [41] See Supplementary Material.
 - [42] N. Laflorencie, Physics Reports **646**, 1 (2016), quantum entanglement in condensed matter systems.
 - [43] L. Amico, R. Fazio, A. Osterloh, and V. Vedral, Rev. Mod. Phys. **80**, 517 (2008).
 - [44] J. Dubail, N. Read, and E. H. Rezayi, Phys. Rev. B **85**, 115321 (2012).
 - [45] A. Sterdyniak, A. Chandran, N. Regnault, B. A. Bernevig, and P. Bonderson, Phys. Rev. B **85**, 125308 (2012).
 - [46] I. D. Rodríguez, S. H. Simon, and J. K. Slingerland, Phys. Rev. Lett. **108**, 256806 (2012).
 - [47] A. Kitaev and J. Preskill, Phys. Rev. Lett. **96**, 110404 (2006).
 - [48] M. Levin and X.-G. Wen, Phys. Rev. Lett. **96**, 110405 (2006).
 - [49] F. D. M. Haldane, Phys. Rev. Lett. **74**, 2090 (1995).
 - [50] P. Calabrese and J. Cardy, Journal of Statistical Mechanics: Theory and Experiment **2004**, P06002 (2004).
 - [51] A. C. Balam, C. Töke, A. Wójs, and J. K. Jain, Phys. Rev. B **92**, 075410 (2015).
 - [52] F. Amet, A. J. Bestwick, J. R. Williams, L. Balicas, K. Watanabe, T. Taniguchi, and D. Goldhaber-Gordon, Nature Communications **6**, 5838 EP (2015), article.
 - [53] B. E. Feldman, A. J. Levin, B. Krauss, D. A. Abanin, B. I. Halperin, J. H. Smet, and A. Yacoby, Phys. Rev. Lett. **111**, 076802 (2013).

- [54] Z. Papić, M. O. Goerbig, and N. Regnault, Phys. Rev. Lett. **105**, 176802 (2010).
- [55] A. Kapustin and N. Saulina, Nucl. Phys. B **845**, 393 (2011).
- [56] X. G. Wen and A. Zee, Phys. Rev. B **46**, 2290 (1992).
- [57] J. Voit, Journal of Physics: Condensed Matter **5**, 8305 (1993).
- [58] T. Giamarchi, *Quantum Physics in One Dimension*, International Series of Monographs (Clarendon Press, 2004).
- [59] D. S. Wei, T. van der Sar, J. D. Sanchez-Yamagishi, K. Watanabe, T. Taniguchi, P. Jarillo-Herrero, B. I. Halperin, and A. Yacoby, Science Advances **3** (2017).
- [60] J. R. Williams, L. DiCarlo, and C. M. Marcus, Science **317**, 638 (2007).
- [61] D. A. Abanin and L. S. Levitov, Science **317**, 641 (2007).
- [62] E. J. Bergholtz and A. Karlhede, Phys. Rev. Lett. **94**, 026802 (2005).
- [63] E. J. Bergholtz and A. Karlhede, Journal of Statistical Mechanics: Theory and Experiment **2006**, L04001 (2006).
- [64] B. A. Bernevig and F. D. M. Haldane, Phys. Rev. B **77**, 184502 (2008).
- [65] B. A. Bernevig and F. D. M. Haldane, Phys. Rev. Lett. **100**, 246802 (2008).
- [66] G. M. Crosswhite, A. C. Doherty, and G. Vidal, Phys. Rev. B **78**, 035116 (2008).
- [67] B. Pirvu, V. Murg, J. I. Cirac, and F. Verstraete, New Journal of Physics **12**, 025012 (2010).
- [68] R. Fern, R. Bondesan, and S. H. Simon, ArXiv e-prints (2018), arXiv:1805.04108 [cond-mat.str-el].
- [69] B. Estienne, N. Regnault, and B. A. Bernevig, Phys. Rev. Lett. **114**, 186801 (2015).

SUPPLEMENTARY INFORMATION

MPS, K Matrix and CFT Hilbert Space Embedding

We first briefly recall the theoretical background concerning the exact MPS description of the Laughlin $1/m$ and the spin singlet Halperin $(m, m, m-1)$ states [34, 36, 37]. The exact MPS description of an FQH state which can be written as a CFT correlator consists of an electronic part and a background part [34, 36]. The former can be deduced from the mode expansion of the primaries appearing in the CFT correlators. The main result of Ref. [37] is a method to determine those primaries and the exact MPS representation of two-components abelian states from a factorization of the \mathbf{K} -matrix as $\mathbf{K} = \mathbf{Q}\mathbf{Q}^T$ [9, 56]. We choose \mathbf{Q} to be upper diagonal for reasons which will become clear later on:

$$\mathbf{K} = \begin{pmatrix} m & m-1 \\ m-1 & m \end{pmatrix}, \quad \mathbf{Q} = \begin{pmatrix} \frac{2m-1}{R_+} & \frac{m-1}{R_-} \\ 0 & \frac{m}{R_-} \end{pmatrix} \quad (5)$$

where we have defined $R_+ = \sqrt{m(2m-1)}$ and $R_- = \sqrt{m}$. The underlying CFT is that of a two component boson (φ^+, φ^-) [30]. Their respective $U(1)$ -charges are integers N_+ , N_- if measured in units of R_+ and R_- respectively, and satisfy the constraint $\frac{N_+ + (m-1)N_-}{m} \in \mathbb{Z}$ [37]. Compared to Ref. [37], Eq. 5 is just a different choice of orthonormal basis for the two-component boson, which is related to the usual spin-charge formulation [57, 58] by:

$$\varphi^+ = \sqrt{\frac{1}{2m}}\varphi^c + \sqrt{\frac{2m-1}{2m}}\varphi^s, \quad \varphi^- = \sqrt{\frac{2m-1}{2m}}\varphi^c - \sqrt{\frac{1}{2m}}\varphi^s \quad (6)$$

We now summarize the results of Ref. [37] using the same notations. We define spinful electronic operators

$$\mathcal{W}^\uparrow(z) =: \exp\left(i\sqrt{\frac{2m-1}{m}}\varphi^+(z) + i\frac{m-1}{\sqrt{m}}\varphi^-(z)\right) : \chi, \quad \mathcal{W}^\downarrow(z) =: \exp(i\sqrt{m}\varphi^-(z)) : \quad (7)$$

where χ acts as a Klein factor ensuring correct commutation relations between the electronic operators (see Ref. [37] for an explicit expression). The j -th Landau orbital on the cylinder is characterized by its occupation numbers n^\uparrow and n^\downarrow . The electronic part $A^{(n^\uparrow, n^\downarrow)}[j]$ of the Halperin MPS matrices only depends on the mode expansion of the electronic operators of Eq. 7:

$$A^{(n^\uparrow, n^\downarrow)}[j] = \frac{1}{\sqrt{n^\uparrow!n^\downarrow!}} \left(\mathcal{W}_{-j}^\uparrow\right)^{n^\uparrow} \left(\mathcal{W}_{-j}^\downarrow\right)^{n^\downarrow} \quad (8)$$

It simply reduces to $A^{(0, n^\downarrow)}[j]$ for the (spin down) polarized Laughlin state. Our variational ansatz relies on the following crucial point: the Laughlin CFT Hilbert space made of a single boson φ^- is embedded into the Halperin CFT Hilbert space. Hence both sets of MPS matrices share the same auxiliary space which makes the gluing procedure straightforward in the Landau orbital basis, *i.e.* a simple matrix multiplication. The basis change of Eq. 6 makes this conformal embedding transparent. At the transition between the Halperin and the spin down polarized Laughlin bulks, the degrees of freedom related to φ^- should gap out [16, 17] because spin down electrons are free to pass through the transition. The one dimensional effective field theory at the transition is thus expected to be the one of a single bosonic φ^+ field, as stated in the main text (see Eq. 3).

To obtain an infinite MPS representation of the states, we combine the electronic operators as $\mathcal{V}(z) = \mathcal{W}^\uparrow(z)|\uparrow\rangle + \mathcal{W}^\downarrow(z)|\downarrow\rangle$. The Operator Product Expansion (OPE) of vertex operators [30] together with the \mathbf{K} -matrix factorization Eq. 5 ensures that the N_e -points correlator

$$\langle \mathcal{O}_{\text{bkg}} \prod_i \mathcal{V}(z_i) \rangle \quad (9)$$

reproduces the Halperin $(m, m, m-1)$ (resp. Laughlin $1/m$) WF with N_e particles through a careful choice of the background charge $\mathcal{O}_{\text{bkg}}^H(N_e) = \exp\left\{-iN_e\frac{2m-1}{2}\left(\frac{1}{R_+}\varphi_0^+ + \frac{1}{R_-}\varphi_0^-\right)\right\}$ (resp. $\mathcal{O}_{\text{bkg}}^L(N_e) = \exp\left\{-iN_e\frac{m}{R_-}\varphi_0^-\right\}$). The choice of the background charge reflects the facts that the Laughlin $1/m$ state is an excitation of the denser Halperin $(m, m, m-1)$ state. Indeed, it may be understood as the introduction of a macroscopic number of φ^+ quasiholes (or a "giant quasihole" [18]) to fully polarize the Halperin Hall droplet into a Laughlin liquid. Spreading these background

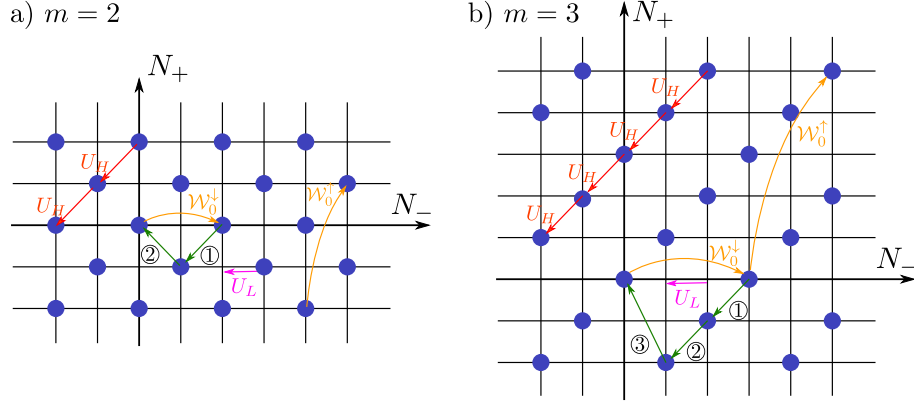


FIG. 4. Charge lattice in the case a) $m = 2$ and b) $m = 3$. The accessible $U(1)$ -charges satisfy the constraint $\frac{N_+ + (m-1)N_-}{m}$ and are shown as blue dots. The action of the electronic operators \mathcal{W}_0^\dagger and \mathcal{W}_0^\downarrow , the Halperin background charge U_H are summarized in orange and red, respectively. The Laughlin background charge U_L (pink) does not link points in the CFT charge lattice. However, we can freely add a shift in N_+ to U_H at each orbital. We tailor this shift such that it is zero after m orbitals as depicted by the sequence a) ①-② and b) ①-②-③ (dark green).

charges equally between the orbitals provides a site-independent MPS representation for the Halperin and Laughlin states on the cylinder. Labeling these site-independent MPS representation B_H and B_L , we have:

$$B_H^{(n^\uparrow, n^\downarrow)} = A^{(n^\uparrow, n^\downarrow)}[0]U_H \quad U_H = e^{-\gamma^2(L_0^+ + L_0^-) - i\left(\frac{\varphi_0^+}{R_+} + \frac{\varphi_0^-}{R_-}\right)} \quad (10a)$$

$$B_L^{(n^\downarrow)} = A^{(0, n^\downarrow)}[0]U_L \quad U_L = e^{-\gamma^2 L_0^- - i\frac{\varphi_0^-}{R_-}} \quad (10b)$$

where we have defined

$$\gamma = \frac{2\pi}{L} \quad (11)$$

L being the cylinder perimeter. Because there is no spin up component in the electronic part of the Laughlin MPS matrices, we may add a shift in the φ^+ $U(1)$ -charge to U_L at each orbital. Doing so allows to always fulfill the compactification constraint $\frac{N_+ + (m-1)N_-}{m} \in \mathbb{Z}$. Since the Laughlin transfer matrix should only be considered over m orbitals not to mix the topological sectors [36], we simply impose this shift in N_+ to be zero every m orbital. One possible way to achieve this is depicted in Fig. 4 together with the action of most operators considered here.

Finite Size Study of the Interface Variational Ansatz

Role of the Boundary States

Eq. 9 shows how the Laughlin $1/m$ state and the Halperin $(m, m, m-1)$ states may be represented as MPS built from the matrices Eq. 10 which share the same auxiliary space. As explained in the main text, our variational ansatz for the interface between the two later consists in gluing these matrices together. Here, we show how this procedure works and we provide a detailed discussion about the role of the MPS boundary states. Let $c_\sigma^\dagger(\mathbf{r})$ be the creation operator of an electron of spin σ at position $\mathbf{r} = (x, y)$. The Lowest Landau Level (LLL) orbitals on the cylinder are:

$$\psi_n(\mathbf{r}) = \frac{e^{ik_n y}}{\sqrt{L\sqrt{\pi}}} e^{-\frac{(x-x_n)^2}{2\ell_B^2}} \quad (12)$$

where the momentum $k_n = \gamma n$ where n is an integer or half an integer, along the compact dimension labels the orbitals and determines the center of the Gaussian envelope

$$x_n = k_n \ell_B^2 \quad (13)$$

TABLE I. Right and left MPS boundary states to recover the glued Laughlin 1/2 and Halperin 221 root partitions. \emptyset , \downarrow and \uparrow respectively denote an empty orbitals or an occupied orbital with a spin down or up. Using the first and the second columns, the total root configuration should be understood as $\dots\emptyset\downarrow\emptyset\downarrow\emptyset\downarrow\emptyset\uparrow\emptyset\uparrow\emptyset\downarrow\dots$ for $[\emptyset-\downarrow]$ and $[\emptyset-\uparrow-\downarrow]$ (e.g. the case shown in the first row). Note that defining the root configuration by, e.g., $[\emptyset-\uparrow-\downarrow]$ instead of $[\emptyset-\downarrow-\uparrow]$ is arbitrary due to the $SU(2)$ singlet nature of the Halperin 221 state.

Root Partition Laughlin	Root Partition Halperin	Boundary U(1) charges (N_-, N_+)
$[\emptyset-\downarrow]$	$[\emptyset-\uparrow-\downarrow]$	$(0, 0)$
$[\emptyset-\downarrow]$	$[\uparrow-\emptyset-\downarrow]$	$(0, 2)$
$[\emptyset-\downarrow]$	$[\uparrow-\downarrow-\emptyset]$	$(0, 4)$
$[\downarrow-\emptyset]$	$[\emptyset-\uparrow-\downarrow]$	$(1, -3)$
$[\downarrow-\emptyset]$	$[\uparrow-\emptyset-\downarrow]$	$(1, -1)$
$[\downarrow-\emptyset]$	$[\uparrow-\downarrow-\emptyset]$	$(1, 1)$

on the cylinder. The corresponding creation operator is $c_{k,\sigma}^\dagger = \int d^2\mathbf{r} \psi_n(\mathbf{r}) c_\sigma^\dagger(\mathbf{r})$. It spans the one-body Hilbert space when k and σ are varied. We consider a system of N_H spin up particles and $N_H + N_L$ spin down particles. A chemical potential is applied to polarize the electrons in the leftmost $N_{\text{orb}}^L = mN_L$ orbitals in their spin down component, while leaving the first $N_{\text{orb}}^H = (2m-1)N_H$ ones unpolarized (see Eq. 1). This may for instance be realized with a gate voltage if the two-level internal degree of freedom physically comes from the valley index in graphene [59–61]. The total background charge required for charge neutrality has two contributions

$$\mathcal{O}_{\text{bkg}} = \mathcal{O}_{\text{bkg}}^H(2N_H) \mathcal{O}_{\text{bkg}}^L(N_L) = \exp \left\{ -iN_{\text{orb}}^H \left(\frac{\varphi_+^0}{R_+} + \frac{\varphi_-^0}{R_-} \right) - iN_{\text{orb}}^L \frac{\varphi_-^0}{R_-} \right\} \quad (14)$$

We denote as $|(n_0^\uparrow, n_0^\downarrow), \dots, (n_{N_{\text{orb}}^H-1}^\uparrow, n_{N_{\text{orb}}^H-1}^\downarrow); n_{(0)}^\downarrow \dots n_{(N_{\text{orb}}^L-1)}^\downarrow\rangle$ the Landau orbitals occupation basis, where we use the compact notation $(i) = N_{\text{orb}}^H + i$ to express the orbital index in the polarized region. Developing our ansatz $|\Psi\rangle = \sum \Gamma_{\{n^\downarrow\}, \{n^\uparrow\}} |\{n^\downarrow\}, \{n^\uparrow\}\rangle$ in this basis leads to a site dependent MPS description with:

$$\Gamma_{\{n^\downarrow\}, \{n^\uparrow\}} = \langle \alpha_L | \mathcal{O}_{\text{bkg}} A^{(0, n_{(N_{\text{orb}}^L-1)}^\downarrow)} [(N_{\text{orb}}^L - 1)] \dots A^{(0, n_{(0)}^\downarrow)} [(0)] A^{(n_{N_{\text{orb}}^H-1}^\uparrow, n_{N_{\text{orb}}^H-1}^\downarrow)} [N_{\text{orb}}^H - 1] \dots A^{(n_0^\uparrow, n_0^\downarrow)} [0] | \alpha_R \rangle \quad (15)$$

where the background charge ensures that $\langle \alpha_L |$ and $|\alpha_R\rangle$ share the same U(1)-charges and conformal dimension. In order to express this MPS with the site independent matrices Eq. 10, we spread the background charge $\mathcal{O}_{\text{bkg}}^H(2N_H)$ over the first N_{orb}^H and $\mathcal{O}_{\text{bkg}}^L$ over the last N_{orb}^L ones. This procedure relies on the translation invariance encoded in the commutation properties of the background charges U_H and U_L (see Refs. [34, 36, 37] for a more thorough study and a careful treatment of geometrical factors). Indeed, they satisfy the following commutation relations

$$U_H A^{(n^\uparrow, n^\downarrow)}[j] U_H^{-1} = A^{(n^\uparrow, n^\downarrow)}[j-1], \quad U_L A^{(0, n^\downarrow)}[j] U_L^{-1} = A^{(0, n^\downarrow)}[j-1] \quad (16)$$

and hence relate the electronic part of the matrices on orbital j to the one on orbital $j-1$. We obtain

$$\Gamma_{\{n^\downarrow\}, \{n^\uparrow\}} = \langle \alpha_L | B_L^{(n_{(N_{\text{orb}}^L-1)}^\downarrow)} \dots B_L^{(n_{(0)}^\downarrow)} B_H^{(n_{N_{\text{orb}}^H-1}^\uparrow, n_{N_{\text{orb}}^H-1}^\downarrow)} \dots B_H^{(n_0^\uparrow, n_0^\downarrow)} | \alpha_R \rangle \quad (17)$$

This iMPS formulation allows to take the limit N_{orb}^L and N_{orb}^H going to infinity and to work on an infinite cylinder, reproducing the bulk physics far from the interface as shown in the main text.

We now focus on the $m=2$ case as in the main text to get a better microscopic understanding of the interface and the role of the MPS boundary conditions quantum numbers. The electronic operators \mathcal{W}^\uparrow and \mathcal{W}^\downarrow generate the charge lattice (see Fig. 4a) from a unit cell composed of 3 inequivalent sites [37]. Physically, they correspond to the ground state degeneracy of the Halperin 221 state on the torus (or infinite cylinder) which is known to be $|\det \mathbf{K}| = 3$ [56]. Hence, the choice of N_+ modulo three determines the topological sector of the Halperin bulk far from the transition. An identical analysis involving the spin down electronic operator \mathcal{W}^\downarrow alone shows that the Laughlin topological sector is selected by the parity of N_- far from the transition on the polarized phase. Loosely speaking, these degeneracies give six different ways of gluing the two bulks together which lead to the observed fractional charge in Fig. 3 and the compactification radius $R_+ = \sqrt{6}$. This intuition is rigorous in the thin torus limit $L \ll \ell_B$ [62, 63] where the bulk physics are dominated by their respective root partitions [64, 65]. In the CFT language, we may understand it as a renormalization procedure. Because the Virasoro zero-th mode L_0 [30] only appears with a prefactor $(\gamma \ell_B)^2$, all

TABLE II. Overlap between the MPS variational ansatz for the $(N_-, N_+) = (0, 0)$ and $P_R = P_L = 0$ boundary conditions and the corresponding ED ground state for different system sizes characterized by the particle numbers $(2N_H, N_L)$. The number of orbitals are fixed to $N_{\text{orb}}^L = 2N_L - 1$ and $N_{\text{orb}}^H = 3N_H$. Due to the dimension of the many-body Hilbert considered (222 415 944 for the largest systems), the overlaps are computed over a significant fraction of the vectors weights. The norms of the truncated ED $|\psi_{\text{trunc}}^{\text{ED}}\rangle$ and MPS $|\psi_{\text{trunc}}^{\text{MPS}}\rangle$ vectors, which can be evaluated rigorously, give an estimate for the possible error.

$(2N_H, N_L)$	$\ \psi_{\text{trunc}}^{\text{ED}}\rangle \ $	$\ \psi_{\text{trunc}}^{\text{MPS}}\rangle \ $	Overlap $ \langle \psi_{\text{trunc}}^{\text{ED}} \psi_{\text{trunc}}^{\text{MPS}} \rangle $
(6,3)	1.00000	1.00000	0.99961
(6,4)	1.00000	1.00000	0.99894
(8,5)	0.99997	0.99997	0.99891

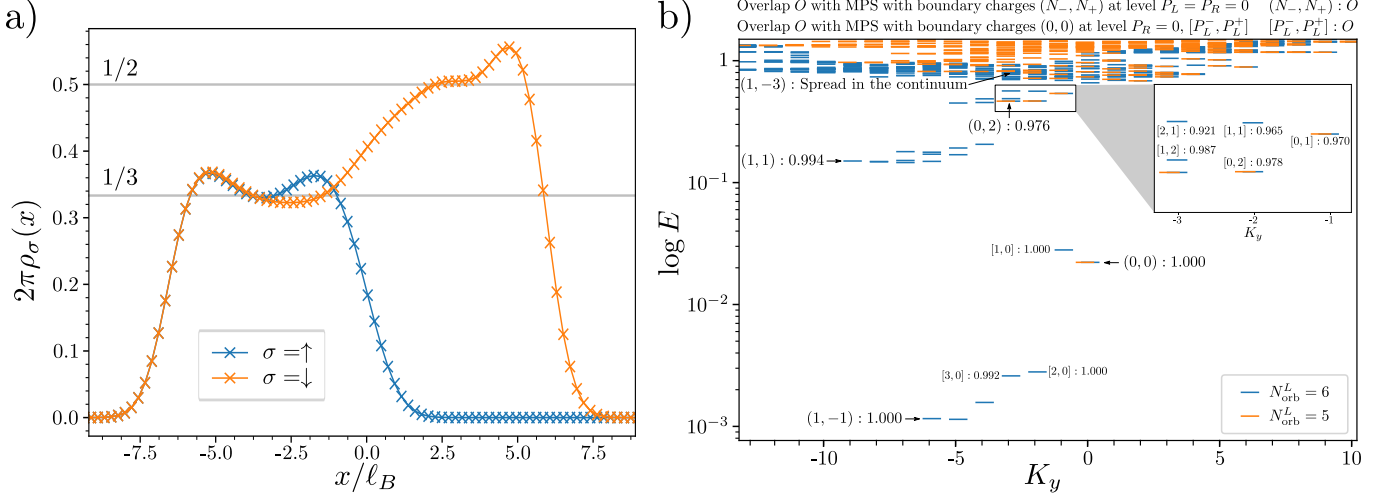


FIG. 5. Finite size investigation of Hamiltonian Eq. 1 with ED. a) Spin resolved density ρ_σ for the ground state for the system described in the main text (second line of Tab. II), i.e. $2N_H = 8$, $N_L = 5$ at $K_y = 10$ ($N_{\text{orb}} = 21$ among which 9 are polarized). For this system sizes, the ED calculation captures both the interface and bulk physics as can be seen from the plateaus of densities at both edges of the sample. b) Energy spectrum (using a logarithmic scale) of Eq. 1 for a system of 6 particles (6 spin down, 3 spin up) on a cylinder of perimeter $L = 9\ell_B$ with $N_{\text{orb}}^H = 9$ orbitals and $N_{\text{orb}}^L = 5$ (orange) or $N_{\text{orb}}^L = 6$ (blue). In the former case, only one of the root configuration of Tab. I can be produced and we can follow interface excitations exactly ($P_L^- = 0$ in square bracket symbols – see text). When $N_{\text{orb}}^L = 6$, excitations of the Laughlin bulk may arise and other root configurations are also possible and are shown with round bracket symbols, together with the overlap with the ED states targeted. We have also indicated in square bracket some excitations for an MPS with boundary charges $(0, 0)$ which reproduce faithfully some of the ED states at low energy. The other low lying states may be reproduced with the same kind of excitations onto MPS with boundary charges $(1, -1)$, $(1, 1)$, $(0, 2)$ and $(0, 4)$. In the later two cases, we should also consider excitations on the Halperin side, i.e. $P_R \neq 0$. Overall, we were able to faithfully capture all the low energy ($E < 0.65$) features of the spectrum with overlaps ranging from 0.921 to 1.000.

excitations becomes highly energetic and we can trace them out. This is exactly what the truncation at $P_{\text{max}} = 0$ does. From here, we may look at the $U(1)$ -charges (N_-, N_+) of the boundary state $|\alpha_R\rangle$ which produce a non-zero coefficient for a given Halperin root partition (i.e. when $P_{\text{max}} = 0$). Depending on the selected root configuration, we have to set the value of $N_+ + 3N_-$ to 0, 2 or 4 on the Halperin side and N_- to 0 or 1 on the Laughlin side. At the transition between the Halperin and Laughlin orbitals, both conditions are met simultaneously, thus fixing completely the $U(1)$ -charges on both sides of the sample for a given pair of Laughlin-Halperin root configurations. The possible choice are summarized in Tab. I. Note that we have never specified the descendant level P_R (resp. P_L) of the state $|\alpha_R\rangle$ (resp. $|\alpha_L\rangle$) for it is fixed by the constraint $P_{\text{max}} = 0$ in the thin torus limit [36, 37]. These insights on the role of boundary states may be used to reproduce the low energy features of finite size systems. The choice of the $U(1)$ -charges selects a root configuration of Tab. I, which fixes the reference for the total angular momentum of the system K_y in finite size. Low energy excitations are obtained by dialing the φ^- and φ^+ descendants.

Comparison with Exact Diagonalization

While our ansatz should capture the low energy physics of the Hamiltonian Eq. 1, we still have to provide convincing numerical evidence. For this purpose, we have performed extensive Exact Diagonalization (ED) of the Hamiltonian Eq. 1 with an infinite chemical potential μ_\uparrow polarizing the first N_{orb}^L orbitals. A typical spectrum is shown in Fig. 5b and exhibits low energy features which clearly detach from the continuum. We would like to show that they can be (partially) captured by our MPS ansatz. Let us first fix the level descendant of the MPS boundary conditions $P_R = P_L = 0$ to describe the states which persist in the thin torus limit $L \ll \ell_B$. The charges of Tab. I select the total momentum of the state along the cylinder perimeter via the root configuration. We observe that, when $N_{\text{orb}}^L = 2N_L - 1$ and $N_{\text{orb}}^H = 3N_H$, the ED ground state has a total momentum equal to the one selected by the $(0, 0)$ boundary charges (see Tab. I and the $N_{\text{orb}}^L = 5$ case in Fig. 5). Our MPS ansatz with these boundary conditions shows extremely high overlap with the corresponding ED ground states (see Tab. II). For the largest reachable system sizes, the spin-resolved densities of the ED ground state depicted in Fig. 5a have a behaviour similar to the one presented in Fig. 1b. They reach plateaus far from the transition, corresponding to the Laughlin and Halperin bulk spin-resolved densities. Hence, both the bulks and interface physics are displayed in the ED study. Its very high overlap with our ansatz shows that this latest correctly captures the interface physics at a microscopic level.

While the ED spectrum does not distinguish between the Laughlin and Halperin bulk excitations and the excitations of interface modes, the high overlap between the MPS states with the low lying part of the ED spectra helps us discriminate these different types of excitations. Thus, we can get some insight of the structure into the spectrum depicted in Fig. 5. To illustrate this, we will first look at the role of the level descendant P_R and P_L when the boundary $U(1)$ -charges are fixed to $(N_-, N_+) = (0, 0)$ and then consider the other gluing conditions of Tab. I. Let us consider for clarity a system of $(2N_H, N_L) = (6, 3)$ particles in $N_{\text{orb}}^L = 2N_L - 1$ and $N_{\text{orb}}^H = 3N_H$ orbitals (orange spectrum in Fig. 5). As stated earlier, the choice in boundary charges $(N_-, N_+) = (0, 0)$ fixes the reference of momentum by selecting a specific root configuration and the ground state corresponds to the case $P_R - P_L = 0$. We note ΔK_y the total momentum relative to the one of the chosen root configuration. We furthermore fix $P_R = 0$ and increase the level descendant of the φ_+ boson in order to excite the interface mode. We thus split $P_L = P_L^- + P_L^+$, where P_L^- (resp. P_L^+) denotes the descendant level of the state α_L with respect to the φ_+ (resp. φ_-) boson. We will label these sectors $[P_L^-, P_L^+]$ (using square brackets). The lowest energy states detaching from the continuum are found to be well captured by the MPS states with boundary condition P_L^+ when the total angular momentum satisfies $\Delta K_y = -P_L^+$ (see the overlaps $[0, P_L^+]$ in Fig. 5). Contrary to bulk excitations, their energies barely change when orbitals are added to the side of the system and they are found to be localized at the interface. This provides another evidence that the interface mode is described by Eq. 3.

Adding an extra orbital on the Laughlin side allows to probe low energy excitations at the edge of the Laughlin bulk. They are characterized by their level descendant P_L^- and capture extremely well the lowest energy states appearing for $N_{\text{orb}}^L = 6$ (see the overlaps $[P_L^-, 0]$ in Fig. 5). More generically, when the momentum transfer $|\Delta K_y|$ is smaller than $N_H = N_L = 3$ the excitations are found to belong to the space spanned by the MPS vectors labeled by the mixed excitations $[P_L^-, P_L^+]$. When $|\Delta K_y|$ is larger, the root partition dominating the low energy feature of the spectrum might change, as in finite size such change only requires a finite momentum transfer. Changing the charge sector as prescribed in Tab. I, we could discriminate between the different gluing conditions Tab. I. The remaining low lying states may be reproduced with the same kind of excitations $[P_L^-, P_L^+]$ onto MPS with boundary charges $(1, -1) - (1, 1) - (0, 2)$ and $(0, 4)$. In the later two cases, one should also consider excitations on the Halperin side, *i.e.* $P_R \neq 0$. Overall, we were able to faithfully capture all the low energy ($E < 0.65$) features of the spectrum with overlaps ranging from 0.921 to 1.000 (as a rule of thumb, the closer to the continuum the poorer the MPS ansatz performs).

Beyond Finite Size: Dispersion Relation of the Interface Gapless Mode

Following Refs. [38–40], we expressed the Hamiltonian Eq. 1 as a Matrix Product Operator (MPO) in order to overcome finite-size effects of ED. For such long range Hamiltonians [27, 28], exact MPO representations involve an infinite bond dimension χ_{MPO} and practical implementations require to approximate the MPO's action on an MPS. An efficient and memory effective way to do so, which dramatically decreases χ_{MPO} compared to other methods [40], is to model the Hamiltonian by a sum of exponentials [66, 67] which possess each a rank 3 MPO representation. Keeping up to 8 exponential terms, we obtained an MPO of bound dimension $\chi_{\text{MPO}} = 936$ which faithfully describe the Hamiltonian Eq. 1 for the perimeters considered. A major advantage of our approach is the ability to focus solely on the edge mode at the interface. Indeed, ED would show the combination of all possible excitations as discussed

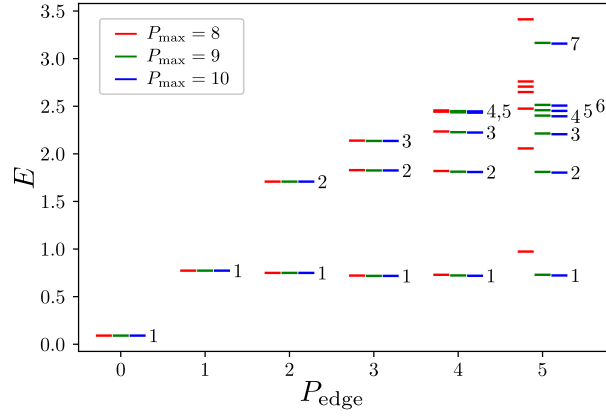


FIG. 6. Energy of the MPS ansatz when momentum excitations of the critical interface mode are controlled via the MPS boundary level descendant P_{edge} on the Laughlin side. The system consists of 60 orbitals (30 on the Laughlin side, 30 on the Halperin side) which is enough to get rid of finite size effects at perimeter $L = 12\ell_B$. The results are shown for three truncation parameters $P_{\text{max}} = 8, 9$ and 10. The counting statistics and the upper linear branch agree with the prediction of Eq. 3.

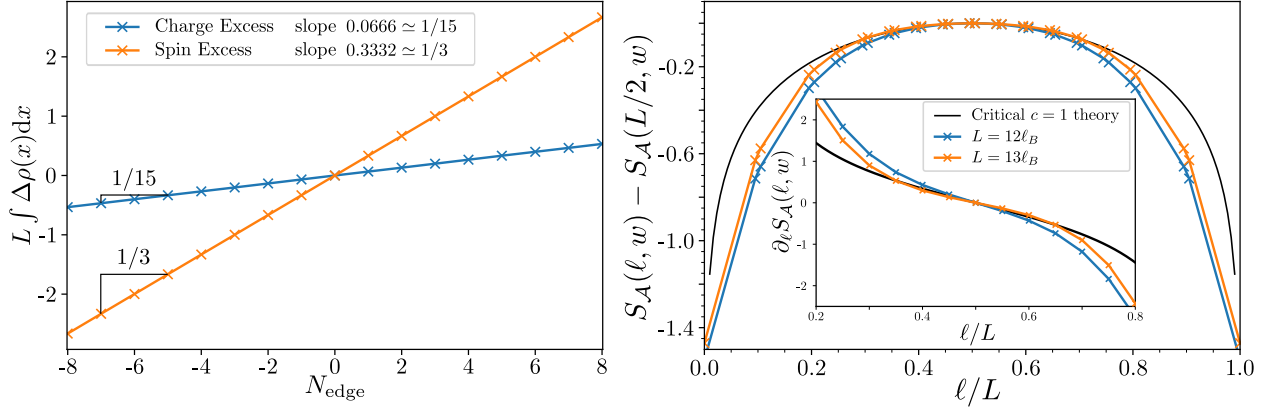


FIG. 7. Numerical results for the transition between the fermionic Laughlin $1/3$ and Halperin 332 states. The conclusions drawn from the bosonic case in the text still apply. A gapless interface mode described by a $c = 1$ CFT appears at the interface. a) It carries fractional charge $e/15$. b) The EE obtained from the Levin Wen subtraction scheme depicted in Fig. 2 for a patch of width $w = 3.25\ell_B$. The trend points toward a $c = 1$ critical theory at the interface, as in the bosonic case. Compared to Fig. 2 in the main text, finite size effects plays are more important because of the larger bulk correlation lengths.

previously, scrambling the dispersion relation of the gapless interface mode. In Fig. 6, we show the dispersion relation of the critical interface mode computed for a system of 60 orbitals (we have checked the convergence with the number of orbitals). It exhibits the counting statistics of a massless boson and a linear upper branch, as expected by the prediction Eq. 3 [30]. The mode velocity is extremely high with a large spread per momentum sector. This explains why the excitations $P_{\text{edge}} > 2$ reach the continuum. We attribute these energetic behaviors to the sharpness of the transition described by our ansatz, *i.e.* to the change from $\mu_{\uparrow} = 0$ to $\mu_{\uparrow} = \infty$ over one inter-orbital distance. Because of the strong and sharp confinement of spin up in the Halperin region, large corrections to this linear behavior are expected due to scattering between the excited modes (see discussion in Ref. [68] for a similar situation). We believe that a smooth transition would provide a more realistic spectrum and a smaller velocity. A corresponding ansatz could be derived by using a similar approach to the RSES, namely a weighted combination of the two types of matrices.

Other Transition: The Fermionic Case

The theory in terms of \mathbf{K} -matrix applies to both bosonic and fermionic systems. Our framework and derivations are applicable to the transition between the fermionic Laughlin $1/3$ and Halperin 332 states. The only challenge is the numerical complexity that quickly increases with larger m values. We give some results on this fermionic interface

in Fig. 7. In that case, finite size effects are more important due to large bulk correlation lengths [37]. However, we can still distinguish the signature of a $c = 1$ critical theory (see Fig. 7). From the fitting procedure described in the main text, we extract a central charge $c = 1.085$ in agreement with Eq. 3. We can also determine the fractional charge by computing densities which quickly converge with respect to P_{\max} . The results shown in Fig. 7a agree with an extremely high accuracy with Eq. 3. Elementary excitations at the transition carries fractional charge $e/15$ and a fractional spin $1/3$ in unit of the electron spin. More generally, the transition between Laughlin $1/m$ state and an Halperin $(m, m, m - 1)$ state should host quasiparticles of charge $e/(m(2m - 1))$.

Entanglement Entropy and MPS: Derivation

We now turn to the computation of the Real Space Entanglement Spectrum (RSES) [44–46] for the two bipartitions discussed in the main text. We recall that the electronic operator modes commute (resp. anti-commute) for bosons (resp. fermions). We will use these relations extensively to compute the RSES. For clarity, we focus primarily on the Laughlin case, the generalization to the Halperin case or to the Laughlin-Halperin interface only involves additional indices without involving any new technical step. For clarity, we will remove the spin index from the discussion whenever they are not needed. We have the following site dependent MPS representation of the Laughlin $1/m$ state [36]:

$$|\Psi_m\rangle = \sum_{\{n_k\}} \langle \alpha_L | \mathcal{O}_{\text{bkg}}^L \left[\prod_{k=0}^{N_\phi} \frac{1}{n_k!} (\mathcal{W}_{-k})^{n_k} \otimes (c_k^\dagger)^{n_k} \right] (|\alpha_R\rangle \otimes |0\rangle) \quad (18)$$

where c_k^\dagger creates a particle of orbital k (see Eq. 12) and $|0\rangle$ denotes the vacuum of the many-body physical space. We have considered a finite size system consisting of $N_{\text{orb}} = N_\phi + 1$ orbitals whose Landau orbitals occupation many-body basis is denoted as

$$|n_0, \dots, n_{N_\phi}\rangle = \prod_{k=0}^{N_\phi} \frac{1}{\sqrt{n_k!}} (c_k^\dagger)^{n_k} |0\rangle \quad (19)$$

The states α_L and α_R belong to the CFT Hilbert space described previously and are characterized by the φ^- U(1)-charge and descendant level. Both states share the same quantum numbers relative to φ^+ because the Laughlin MPS matrices act as the identity on this bosonic degrees of freedom. α_L and α_R can first be imagined to be in the CFT vacuum state. The afore-mentioned site independent MPS representation Eq. 10 comes from the spreading of the background charge [34] and requires a shift of the MPS-boundary state U(1) charges [36], which we will keep implicit here:

$$\chi_{\{n\}} = \langle \alpha'_L | B_L^{(n_{N_\phi})} \dots B_L^{(n_0)} | \alpha'_R \rangle \quad (20)$$

Real Space Bipartition

Consider now a generic real space bipartition $\mathcal{A} - \mathcal{B}$, the LLL orbitals Eq. 12 are decomposed as $c_k^\dagger = d_{k,\mathcal{A}}^\dagger + d_{k,\mathcal{B}}^\dagger$ with

$$d_{k,\mathcal{I}}^\dagger = \int_{\mathbf{r} \in \mathcal{I}} d^2\mathbf{r} \psi_k(\mathbf{r}) c_k^\dagger(\mathbf{r}), \quad \mathcal{I} \in \{\mathcal{A}, \mathcal{B}\} \quad (21)$$

The sets $\{d_{k,\mathcal{A}}\}$ and $\{d_{k,\mathcal{B}}\}$ spans two disjoint Hilbert spaces of respective vacua $|0_{\mathcal{A}}\rangle$ and $|0_{\mathcal{B}}\rangle$ but are in general not orthogonal nor orthonormal:

$$[d_{k,\mathcal{I}}, d_{\ell,\mathcal{I}'}^\dagger]_m = \delta_{\mathcal{I},\mathcal{I}'} \int_{\mathbf{r} \in \mathcal{I}} d^2\mathbf{r} \psi_k^*(\mathbf{r}) \psi_\ell(\mathbf{r}) \quad (22)$$

where $[\cdot, \cdot]_m$ denotes the commutator (resp. anticommutator) if m is even (resp. odd). For a cut preserving the rotation symmetry along the cylinder perimeter $\mathcal{A} = \{(x, y) | x < x_0, 0 \leq y \leq L\}$, the overlaps in the right hand side of Eq. 22 are diagonal and take the form

$$g_{k,\mathcal{A}} = \int_{\mathbf{r} \in \mathcal{A}} d^2\mathbf{r} \psi_k^*(\mathbf{r}) \psi_k(\mathbf{r}) = \sqrt{\frac{1}{\pi \ell_B} \int_{x < x_0} dx \exp\left(-\frac{(x - x_k)^2}{\ell_B^2}\right)} \quad (23)$$

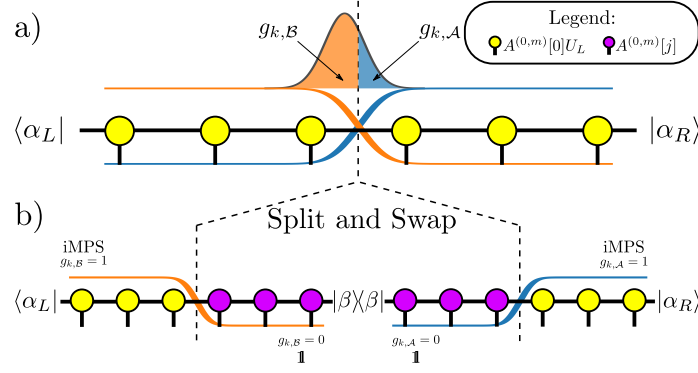


FIG. 8. a) For a rotationally symmetric cut perpendicular to the cylinder axis, the Landau orbitals are split into two. The cut is shown as a dashed black line. The weight $g_{k,A}$ and $g_{k,B}$ (see Eq. 23) are depicted graphically in respectively in blue and orange. The graphical representation of the site independent MPS is also depicted. b) After the split and swap procedure, we obtain a Schmidt decomposition (see Eq. 25). The cut breaks the translation symmetry along the cylinder axis, which is encoded in the properly weighted site dependent matrices used (purple) near the cut. Far away from the cut, we can switch to the iMPS matrices exactly and hence perform calculation in the thermodynamic limit.

in part \mathcal{A} while normalization requires $g_{k,B} = \sqrt{1 - g_{k,A}^2}$. These overlaps can still be computed analytically for some bipartitions breaking the rotation symmetry such as the ones described in the text (see Fig. 2). Hence, $\{d_{k,A}\}$ may be decomposed over an orthonormal basis $\{\tilde{c}_{\mu,A}\}$ as

$$d_{k,A}^\dagger = \sum_{\mu=0}^{N_\phi} \alpha_{k,\mu} \tilde{c}_{\mu,A}^\dagger \quad (24)$$

where the coefficient $\{\alpha_{k,\mu}\}$ are obtained either analytically or numerically from the known overlaps between LLL orbitals over the region \mathcal{A} .

Split and Swap Procedure

Using the decomposition $c_k^\dagger = d_{k,A}^\dagger + d_{k,B}^\dagger$ together with the commutation relations of Eq. 22, and introducing a closure relation $\sum_{\beta \in \mathcal{H}_{\text{CFT}}} |\beta\rangle\langle\beta|$, with \mathcal{H}_{CFT} the auxiliary space, *i.e.* the CFT Hilbert space, Eq. 20 is found to have the following Schmidt decomposition onto the partition $\mathcal{A} - \mathcal{B}$:

$$|\Phi_{\alpha_R}^{\alpha_L}\rangle = \sum_{\beta \in \mathcal{H}_{\text{CFT}}} |\phi_\beta^{\mathcal{B}}\rangle \otimes |\phi_\beta^{\mathcal{A}}\rangle \quad (25)$$

with:

$$\begin{aligned} |\phi_\beta^{\mathcal{B}}\rangle &= \sum_{\{n_k^{\mathcal{B}}\}} \langle \tilde{\alpha}_L | \left[\prod_{k=0}^{N_\phi} \frac{1}{n_k^{\mathcal{B}}!} (\mathcal{W}_{-k})^{n_k^{\mathcal{B}}} \otimes (d_{k,B}^\dagger)^{n_k^{\mathcal{B}}} \right] (|\beta\rangle \otimes |0_{\mathcal{B}}\rangle) \\ |\phi_\beta^{\mathcal{A}}\rangle &= \sum_{\{n_k^{\mathcal{A}}\}} \langle \beta | \left[\prod_{k=0}^{N_\phi} \frac{1}{n_k^{\mathcal{A}}!} (\mathcal{W}_{-k})^{n_k^{\mathcal{A}}} \otimes (d_{k,A}^\dagger)^{n_k^{\mathcal{A}}} \right] (|\alpha_R\rangle \otimes |0_{\mathcal{A}}\rangle) \end{aligned} \quad (26)$$

where we have set $\langle \tilde{\alpha}_L | = \langle \alpha_L | \mathcal{O}_{\text{bkg}}^L$. Thus, we have split the MPS, corresponding to the two subsystems \mathcal{A} and \mathcal{B} ("split" procedure in Fig. 8). This step is described in more detailed for the rotationally symmetric case in Ref. [34, 37].

From now on, we focus on subspace \mathcal{A} , the derivation being exactly the same for the subspace \mathcal{B} . The occupation numbers $\{n_k^{\mathcal{A}}\}$ are equivalently described by ordered lists of occupied orbitals $\lambda = (\lambda_1, \dots, \lambda_{N_e})$, with N_e the number of electrons in the system:

$$N_\phi \geq \lambda_1 \geq \dots \geq \lambda_{N_e} \geq 0 \quad \text{for bosons,} \quad (27a)$$

$$N_\phi \geq \lambda_1 > \dots > \lambda_{N_e} \geq 0 \quad \text{for fermions.} \quad (27b)$$

Because of the commutation relation of the vertex operator modes, we may also write

$$|\phi_\beta^A\rangle = \sum_{\lambda_1, \dots, \lambda_{N_e}} \langle \beta | \left[\prod_{j=1}^{N_e} \mathcal{W}_{-\lambda_j} \otimes d_{\lambda_j, A}^\dagger \right] (|\alpha_R\rangle \otimes |0_A\rangle) \quad (28)$$

where the sum runs over unordered lists of integers $\{\lambda\}$. Plugging the orthonormal basis with Eq. 24 and reordering the various terms, we find

$$|\phi_\beta^A\rangle = \sum_{\mu_1, \dots, \mu_{N_e}} \langle \beta | \left[\prod_{j=0}^{N_\phi} \left(\sum_{\lambda=0}^{N_\phi} \alpha_{\lambda, \mu_j} \mathcal{W}_{-\lambda} \right) \otimes \tilde{c}_{\mu_j, A}^\dagger \right] (|\alpha_R\rangle \otimes |0_A\rangle) \quad (29)$$

A similar reasoning helps us to finally expressing the state $|\phi_\beta^A\rangle$ in the occupation basis relative to the new physical space spanned by the orthonormal basis $\{\tilde{c}_{k, A}\}$. We find the MPS expression

$$|\phi_\beta^A\rangle = \sum_{\{n_k^A\}} \langle \beta | K_{\mathcal{A}}^{n_{N_\phi}^A} [N_\phi] \cdots K_{\mathcal{A}}^{n_0^A} [0] |\alpha_R\rangle |n_{N_\phi}^A \cdots n_0^A\rangle, \quad K_{\mathcal{A}}^n[j] = \frac{1}{\sqrt{n!}} \left(\sum_{\lambda=0}^{N_\phi} \alpha_{\lambda, j} \mathcal{W}_{-\lambda} \right)^n \quad (30)$$

Here, we have used the commutation relations of the vertex operator modes to swap the matrices in order to derive Eq. 30, an site dependent representation of $|\phi_\beta^A\rangle$ onto the orthonormal basis $\{\tilde{c}_{k, A}\}$.

Spreading the Background Charge

The last step of the derivation consists in spreading the background charge in order to find back the iMPS matrices Eq. 10 far away from the cut. The Laughlin background charge $\mathcal{O}_{\text{bkg}}^L$ can only be spread over N_{orb} orbitals, but the bipartition has introduced twice more matrices (N_{orb} in both parts \mathcal{A} and \mathcal{B}). Although any repartition of the background charge over these matrices is acceptable, we append U_L to the first (resp. last) $N_{\text{orb}}/2$ matrices of \mathcal{A} (resp. \mathcal{B}). Using the relations of Eq. 16, the product of matrices appearing in Eq. 30 can be split into two parts

$$\left(F_{\mathcal{A}}^{(n_{N_\phi}^A)} [N_\phi, N_{\text{orb}}/2] \cdots F_{\mathcal{A}}^{(n_{N_{\text{orb}}/2}^A)} [N_{\text{orb}}/2, 1] \right) \left(F_{\mathcal{A}}^{(n_{N_{\text{orb}}/2-1}^A)} [N_{\text{orb}}/2 - 1, 0] U_L \cdots F_{\mathcal{A}}^{(n_0^A)} [0, 0] U_L \right) \quad (31)$$

where we have defined

$$F_{\mathcal{A}}^{\tilde{n}}[j, q] = \frac{1}{\sqrt{\tilde{n}!}} \left(\sum_{\lambda=0}^{N_\phi} \alpha_{\lambda, j} \mathcal{W}_{-(\lambda-j)+q} \right)^{\tilde{n}} \quad (32)$$

For a partition preserving the rotation symmetry around the cylinder axis, we have $\alpha_{k, r} = \delta_{k, r} g_{k, A}$ (see Eq. 23) and we thus recover the tensor of Refs. [34, 36, 37]. For the rectangular patch described in the main text, the off diagonal weights $\alpha_{k, r}$ decay rapidly for orbitals far from the cut (typically like Gaussian multiplied by cardinal sine functions) so that we can approximate $\alpha_{k, r} \simeq \delta_{k, r} g_{k, A}$. In other words, the rotation symmetry is recovered after a large enough number of orbitals. Moreover, far away from the cut in the iMPS part of the product, $g_{k, A} = 1$ and we get back the site independent matrices $F_{\mathcal{A}}^{(n)}[k, 0] U_L = B_L^{(n)}$. Similarly when $g_{k, A} = 0$, *i.e.* far away from the cut in the site-dependent part of the product, the matrices reduces to $F_{\mathcal{A}}^n[j, q] \simeq \delta_{n, 0} \mathbb{1}$, with $\mathbb{1}$ being the identity operator over the auxiliary space. This shows that the translation invariance along the cylinder axis is recovered far away from the transition. We can thus work on the infinite cylinder and take $N_{\text{orb}} \rightarrow +\infty$, by switching to the site independent matrices far away from the cut. The situation is depicted in Fig. 8b. Numerically, we have considered up to 50 orbitals in the site-dependent region to ensure that when the iMPS is glued to take the limit $N_{\text{orb}} \rightarrow +\infty$, we always satisfy the condition $|\alpha_{k, r} - \delta_{k, r}| < 10^{-10}$.

Entanglement Entropy and MPS: Numerical Results

We now go back to the transition between the Laughlin 1/2 and Halperin 221 states described in the main text. We choose the origin for the x -axis between the Laughlin and Halperin orbitals, *i.e.* the center of the LLL orbitals

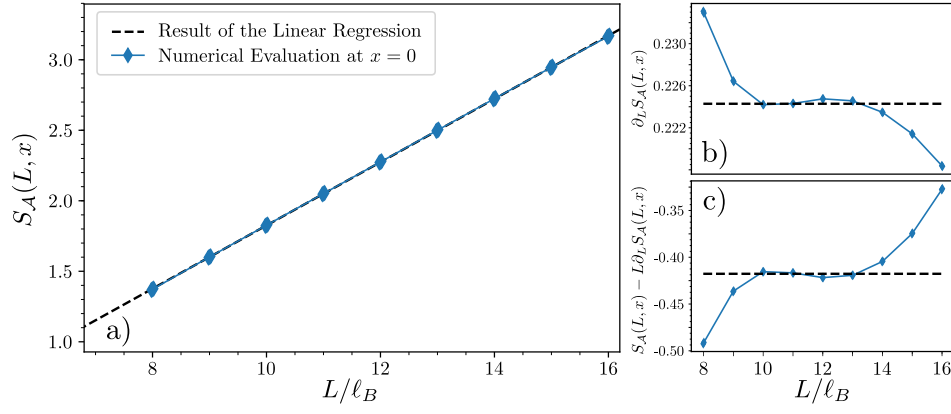


FIG. 9. a) The EE $S_A(L, x)$ shows perfect agreement with the area law of Eq. 33 – here illustrated for $x = 0$ and computed for a truncation parameter $P_{\max} = 12$. Comparison between the numerical evaluation of b) $\alpha(x) = \partial_L S_A(L, x)$ and c) $\gamma(x) = S_A(L, x) - L \partial_L S_A(L, x)$ with finite differences and the results of the linear regression. Both are constant over the range of perimeters $L \sim 10 - 13\ell_B$ where both finite size effects and saturation effects due to the finite bond dimension are controlled.

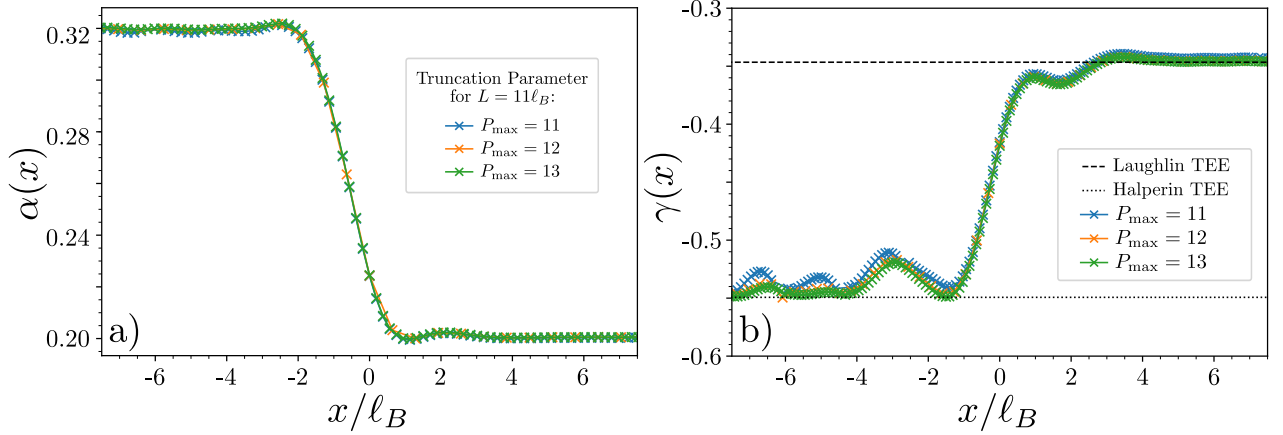


FIG. 10. Convergence of the numerically extracted a) $\alpha(x)$ and b) $\gamma(x)$ at $L = 12\ell_B$ with respect to the truncation parameter P_{\max} . As expected, the subleading term $\gamma(x)$ is more affected by the saturation effects, especially in the region where $\alpha(x)$ is large. This occurs on the Halperin side, i.e. $x < 0$. Note that the results of b) for $P_{\max} = 13$ are already shown in the main text.

for which Laughlin (resp. Halperin) iMPS matrices are used are $x_n = \gamma(n + 1/2)\ell_B^2$ (resp. $x_n = -\gamma(n + 1/2)\ell_B^2$) with $n \in \mathbb{N}$. We apply the previous formalism for the cut $\mathcal{A} = \{(x', y') | x' < x, 0 \leq y' \leq L\}$, which is rotationally invariant along the cylinder perimeter. We numerically compute the RSES and the corresponding Von Neumann EE $S_A(L, x)$ for various cylinder perimeters L . As claimed in the main text, we always observe an area law behavior for which the first correction is constant

$$S_A(L, x) = \alpha(x)L - \gamma(x) \quad (33)$$

This linear behavior is well satisfied numerically as shown for a cut at $x = 0$ in Fig. 9a. In Fig. 9b and c, we compare the results of the linear regression with the numerical evaluation of $\alpha(x) = \partial_L S_A(L, x)$ and $\gamma(x) = S_A(L, x) - L \partial_L S_A(L, x)$ with finite differences. The corrections to these constants are of subleading order, and are much more sensitive to finite size effects ($L \leq 9\ell_B$ on Fig. 9) or to saturation effects due to the truncation of the auxiliary space ($L \geq 15\ell_B$ on Fig. 9). The later point is easily understood when noticing that in order to faithfully describe a state satisfying Eq. 33, the bond dimension χ of the MPS should grow exponentially with the cylinder perimeter $\chi \sim e^{\alpha(x)L}$. However, we notice that in the range $L \simeq 11 - 13\ell_B$, we may reliably use either techniques (fit or discrete derivative) to compute the coefficients $\alpha(x)$ and $\gamma(x)$. These are the perimeters we extensively use in the main text and thereafter.

In particular, we focus on $L = 11\ell_B$ and study the convergence of the numerically extracted $\alpha(x)$ and $\gamma(x)$ near the transition. Fig. 10 shows the numerical results for $x \in [-7.5, 7.5]$ (we refer to Ref. [37] for a similar analysis deep in the bulks). We observe that the greater $\alpha(x)$ and the more sensitive $\gamma(x)$ is to saturation effects. This agrees

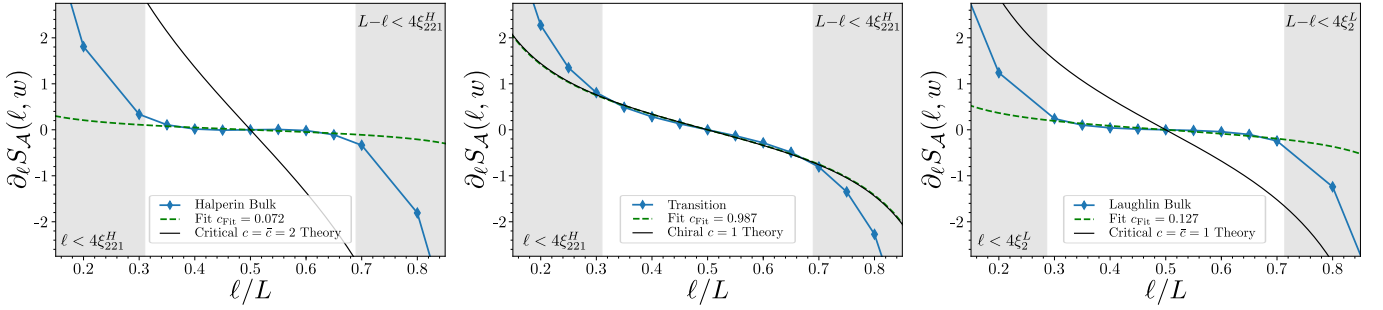


FIG. 11. Fitting procedure to characterize the critical contribution to the EE $S_A(\ell, w)$ for a Levin-Wen type cut depicted in Fig. 2 a) far in the Halperin bulk, b) for a patch covering the transition and c) deep in the Laughlin phase. All data points were taken for a cylinder perimeter $L = 12\ell_B$, a patch width $w = 2.75\ell_B$ and a truncation parameter $P_{\max} = 12$. To mitigate finite size effects, we discard the points for which ℓ or $L - \ell$ are smaller than four times the correlation length (grey shaded area in the plots). We took the bulk Halperin 221 correlation length $\xi_{221}^H \simeq 0.941\ell_B$ in a) and b) and the Laughlin $1/2$ bulk correlation length $\xi_2^L \simeq 0.858\ell_B$ which we had previously extracted [37]. We only see a critical contribution when the patch covers the transition region and is large enough (see Fig. 12), as expected.

with our previous discussion on the required bound dimension required to attain convergence $\chi \sim e^{\alpha(x)L}$. Note that the truncation parameter P_{\max} is a logarithmic measure of the bound dimension [36] and that the computation for $P_{\max} = 13$ requires an auxiliary space of dimension $\chi = 41\,558$.

Levin-Wen Subtraction Scheme

In the main text, we consider the RSES for a bipartition consisting of a rectangular patch of width $w = x_{\text{stop}} - x_{\text{start}} > 0$ along the cylinder axis and a length $\ell \in [0, L]$ around the cylinder perimeter, $y_{\text{stop}} = -y_{\text{start}} = \ell/2$. A half infinite cylinder is added to the patch (see Fig. 2 in the main text) in order to be able to switch from a site-dependent and weighted MPS to the iMPS matrices as explained in previous sections. We first would like to qualitatively enumerate the possible contributions to the EE for such a cut. We see three possible contributions [42, 50] for the left topmost cut of Fig. 2

$$\underbrace{\alpha(x_{\text{start}})\ell + \alpha(x_{\text{stop}})(L - \ell) + 2 \int_{x_{\text{start}}}^{x_{\text{stop}}} \alpha(u)du}_{\text{Area Law}} + \underbrace{\frac{c}{6} \log \left[\sin \left(\frac{\pi\ell}{L} \right) \right]}_{\text{Critical Mode}} + K(w) \quad (34)$$

where $K(w)$ is a constant arising from possible correction to the area laws and from the corner contributions. The addition subtraction scheme described in the main text, which is nothing but a Levin-Wen type cut [48], removes the area law terms at x_{start} and x_{stop} together with the corner contributions. Hence, up to a constant $f(w)$ which depends on w , we expect the resulting EE $S_A(\ell, w)$ to have the following form:

$$S_A(\ell, w) = 2 \frac{c}{6} \log \left[\sin \left(\frac{\pi\ell}{L} \right) \right] + f(w) \quad (35)$$

By considering $S_A(\ell, w) - S_A(L/2, w)$, we get rid of $f(w)$ and we obtain Eq. 4 in the main text. This latest has a very good agreement with the results presented in Fig. 2. In the following, we focus on the derivative $\partial_\ell S_A(\ell, w)$ for which the constants or any pure function of w disappear. It allows a one-parameter fit of the numerical data on the theoretical prediction. The fitting procedure described in the main text is exemplified in Fig. 11 where we clearly see that the critical contribution to $\partial_\ell S_A(\ell, w)$ is only present when the patch covers the transition. Deep in either of the two bulks, we indeed only expect area law contributions to the EE and the extraction of the central charge gives $c_{\text{Fit}} = 0.072$ (resp. $c_{\text{Fit}} = 0.127$) deep in the Halperin (resp. Laughlin) phase. This consistency check indicates that the features observed at the transition are not a mere artifact of our numerical analysis.

Covering Entirely the Critical Mode

We first assert that the identification of a $c = 1$ theory at the interface does not depend on finely tuned parameters. The choice of the perimeter is only motivated by the avoidance of finite size effects, as seen on Fig. 2 in the main text.

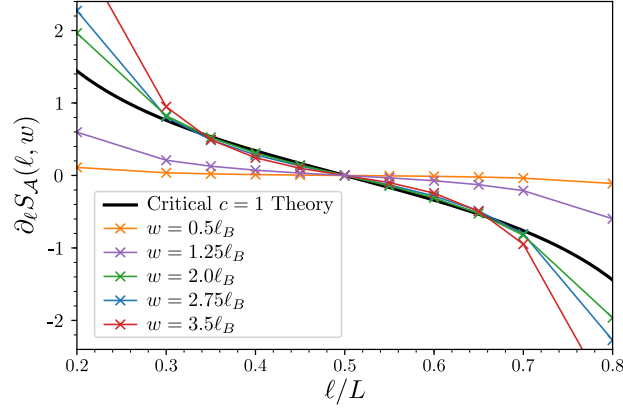


FIG. 12. Derivative of the EE computed with the Levin Wen scheme described in the text for different width of the patch across the transition. For $w \in \{0.5, 1.25, 2.0, 2.75, 3.5\}$, the fitted central charge are respectively 0.04, 0.26, 1.03, 0.99, 1.08. Either the patch is large enough to entirely cover the critical mode $w \geq 2\ell_B$ and the central charge extracted is close to one, or it misses completely or part of the critical mode and we find $c < 1$. This study quantitatively shows that the central charge estimation provided in the main text does not come from a fine tuned choice of our patch.

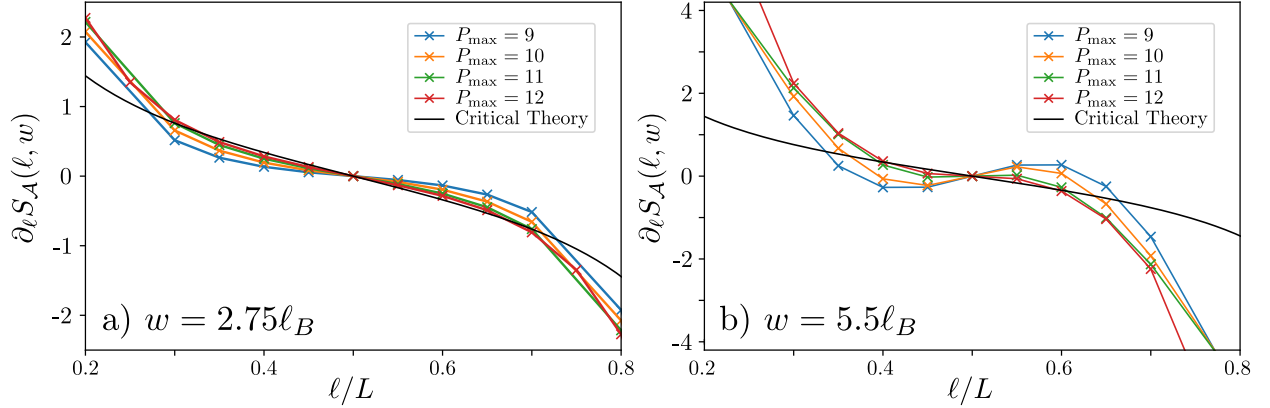


FIG. 13. Convergence of the derivative of the EE with respect to the truncation parameter P_{\max} . a) When w is small, the contribution of the critical mode at the interface to the EE may be extracted when the area law contribution are minimal (here for $w = 2.75\ell_B$). b) Saturation effects dominates when the width w is increased. Indeed, it leads to a higher area law contribution along x , requiring an even larger truncation parameter P_{\max} (here for $w = 5.5\ell_B$).

The patch may however not fully cover the critical mode and the extracted value of c be a fraction of the real central charge of the underlying interface theory. To investigate this, we varied the width of the patch over a few magnetic length. For each value of w depicted in Fig. 12, we fit the central charge with the previously described method. We observe that the fitted central charge increases (respectively 0.04 and 0.26 for $w = 0.5\ell_B$ and $w = 1.25\ell_B$) to reach a constant value around one for w large enough (respectively 1.03, 0.99 and 1.08 for $w \in \{2, 2.75, 3.5\}$). This reliably point toward a critical theory of central charge $c = 1$, which is only entirely capture when the patch is wide enough to fully cover the gapless interface mode. Note that higher values of w are plagued by the finite auxiliary space dimension: Increasing w leads to a higher area law contribution along x , requiring an even larger truncation parameter P_{\max} . The first signals of such saturation effects are seen for $w = 3.5\ell_B$ in Fig. 12 are investigated further in the next subsection.

Truncation Effects

To exemplify saturation effects, we consider two patches of respective width $w = 2.75\ell_B$ and $w = 5.5\ell_B$. The numerical analysis described in the main text is performed and the results are presented in Fig. 13. The bond dimension required to faithfully capture the entanglement properties, especially the subleading logarithmic term coming from the gapless mode at the interface, grows exponentially with the width of the patch (see discussion above). We indeed see

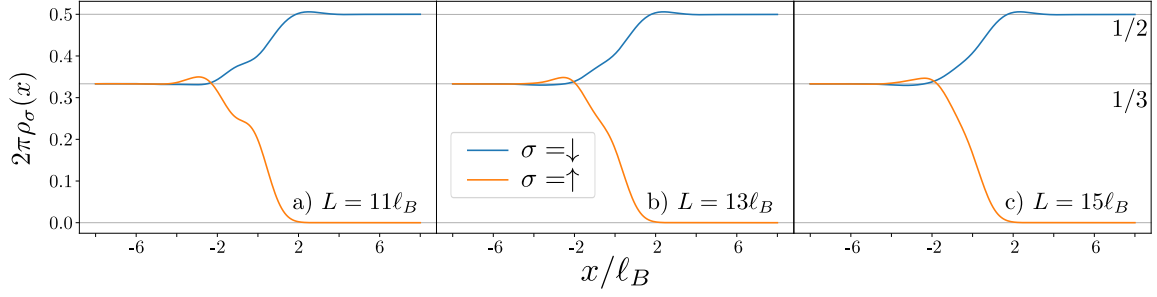


FIG. 14. *Spin resolved densities across the transition for different cylinder perimeters L . The ripples at the transition disappear quickly when the perimeter increases.*

that when $w = 2.75\ell_B$ the EE converges to the theoretical prediction of Eq. 4 with increasing truncation parameter P_{\max} , up to finite size effects when the patch is smaller than or comparable to the bulks correlation lengths. When $w = 5.5\ell_B$, the area law contributions in the x direction are not fully accommodated by the finite auxiliary space and saturation effects dominate. Hence, the EE for finite auxiliary space and large patch deviates from Eq. 4, even if the trend seems to indicate that it will converge to the expected behavior with increasing P_{\max} .

Finite Size Effects - Density

The bulk Laughlin and Halperin correlation lengths in our system may be computed numerically [37, 69], we find them to be slightly smaller than a magnetic length. The thermodynamic limit is reached when the cylinder perimeter is much larger than the later. This is not entirely the case for the perimeters considered, as depicted in Fig. 14. The leftmost plot is the one of Fig. 1b in the main text and corresponds to the typical perimeter used in our simulations. The two other graphs show that the ripples observed at the transition quickly disappear with the cylinder perimeter increases and are finite size effects.

Though present in our simulations, we mitigate finite size effects by only considering objects twice or three times greater than the bulks correlation length. The main limitation comes from the truncation of the auxiliary space and the saturation effects presented above. Note that the density is a more robust quantity that quickly converges with respect to the truncation parameter P_{\max} . So we can safely consider larger perimeters for the density.